Integrated tunable silicon photonic devices for optical filter and delay applications

Linjie Zhou, Xiaomeng Sun, Jingya Xie, Liangjun Lu, Zhi Zou, and Jianping Chen
State Key Laboratory of Advanced Optical Communication Systems and Networks
Department of Electronic Engineering, Shanghai Jiao Tong University, Shanghai 200240, China

Email: ljzhou@sjtu.edu.cn

ABSTRACT

We present our recent work on integrated silicon photonic devices for optical filter and delay applications. A microdisk resonator integrated with interleaved p-n junctions is demonstrated. The resonance can be both blue- and red-shifted by applying a forward current or a negative voltage, respectively. A MZI-nested microring resonator is shown capable of coupling tuning, enabled by a p-i-p junction based thermal heater across the waveguide. We also investigate cascaded self-coupled optical waveguide (SCOW) resonators. Electromagnetically-induced transparency (EIT)-like resonances are generated featuring a narrow lineshape and a high group delay. Finally, we present an athermal lattice filter made up of 10 cascaded Mach-Zehnder interferometer (MZI) units and show that the temperature sensitivity can be considerably reduced.

Keywords: silicon photonics, filters, microresonators, optical delay, optical signal processing, electromagnetically induced transparency

1. INTRODUCTION

Silicon photonics has become an enabling technology for large-scale integrated photonic circuits for applications ranging from long-haul communications to short-reach interconnects [1-3]. Silicon as a photonic material provides multiple advantages to other material systems, such as compact size, low loss, easy integration with microelectronics etc. The compatibility with complementary metal-oxide-semiconductor (CMOS) technologies makes silicon photonic devices suitable for low-cost and high-volume mass production [4, 5]. A variety of silicon photonic devices have been demonstrated in the past decade, including filters [6, 7], switches [8], arrayed waveguide gratings (AWGs) [9], modulators [10-13] etc. Active optical devices like detectors and lasers are also essential for transceivers and other more complicated integrated systems [14, 15]. Germanium is often epitaxially grown on silicon to make photon-detectors using butt or evanescent coupling [16]. As for lasers, although germanium can emit light by strain engineering and under high doping, its threshold current is very high, not ready for practical use [17]. A more practical way to fabricate lasers on silicon is to use hybrid bonding of InP gain material [18].

Of the various devices, microresonators are one of the key components for they can considerably reduce device sizes and power consumption, and meanwhile enhance interaction between light and material. Microrings [19], microdisks [13, 20], Bragg gratings [21], and photonic crystals [22] are the commonly used resonant structures on chip. Thermo-optic effect and free-carrier plasma dispersion effect are the two effects routinely exploited in device tuning. To realize thermal tuning, a thin metal layer with a high resistivity could be deposited on top of devices [23]. Thermal tuning is a very effective way but it has a relatively low response speed and high power consumption. To enable fast tuning, the free-carrier plasma dispersion effect could be used [24]. And indeed, high-speed optical modulators have been implemented based on this effect with carefully designed structures [10-12]. The shortcoming for this effect is that it will bring additional absorption loss with a high concentration of free carriers. This limits its use in devices where only a small refractive index change is needed.

Here we present our recent process on tunable silicon photonics devices with a focus on their filtering and group delay responses. First, we investigate a microdisk resonator integrated with interleaved p-n junctions. Mode dependent

Silicon Photonics VIII, edited by Joel Kubby, Graham T. Reed, Proc. of SPIE Vol. 8629,
86290M · © 2013 SPIE · CCC code: 0277-786X/13/$18 · doi: 10.1117/12.2006143

responses are characterized. We then present a MZI-nested microring resonator whose coupling can be conveniently controlled by thermal heaters formed by the MZI arm waveguides. In the next device, we discuss a novel resonator based on a self-coupled optical waveguide (SCOW). The cascaded SCOW resonators exhibit electromagnetically-induced transparency (EIT)-like resonances with a high Q-factor and a large group delay. Finally, lattice filters consisting of 10 concatenated Mach-Zehnder interferometers (MZIs) are demonstrated to have very low temperature sensitivity owing to the thermally balanced design of MZI units.

2. TUNABLE SILICON PHOTONIC DEVICES

The silicon photonic devices presented here are all made using a CMOS compatible fabrication process. The devices were fabricated on SOI wafers with the top silicon layer 220 nm thick and lightly p-type doped. Ridge-type waveguides are used in our devices with a thin slab of 60 nm for lateral p- or n-type doping. A 1.5 μm silicon dioxide layer is clad on top the waveguides and aluminum wires are used for electrical connection. The devices are characterized using an Agilent loss and dispersion analyzer (86038B). A tunable laser source is first modulated by an RF signal. The modulated light then passes through the devices and the output optical signal is detected and converted back to an electrical one. The electrical signal is compared with a reference RF signal and the transmission loss and phase information are extracted. Only transverse-electric (TE) polarization is measured for our devices. Optical group delay is calculated from the phase response of the devices.

2.1 Tunable microdisk resonator

Figure 1(a) shows the schematic structure of a tunable microdisk resonator integrated with interleaved p-n junctions along its rim. The access waveguide width is 0.4 μm. The microdisk has a diameter of 12 μm and the gap separation from the waveguide is 0.25 μm. The p-n junctions have a doping concentration of ~10^{17} cm^{-3}. Highly doped P^+ and N^+ regions with a concentration of ~10^{20} are positioned outside and inside the disk respectively for good ohmic contact with aluminum wire connections. The distance of the P^+ doping to the disk rim is 0.6 μm and that of the N^+ doping is 1.8 μm. As the whispering-gallery modes (WGMs) in the microdisk has its mode field concentrated near the rim, the N^+ doping position can be optimized such that it will not significantly affect the lower-order WGMs. On the contrary, higher-order WGMs could be partially suppressed by the doping [13]. Here we use the interleaved p-n junctions because they can be both forward- and reverse-biased to get blue- and red-shift of the resonances, respectively. Compared to a single circular p-n junction along the disk rim, the interleaved p-n junctions have higher tuning efficiency and higher tolerance to overlay misalignment in fabrication [12]. Moreover, the interleaved p-n junctions have a potentially high response speed. Figure 1(b) shows the microscope image of the fabricated device.

Figure 1(c) illustrates the measured transmission spectrum of the microdisk resonator. Three WGMs labeled as A, B, and C are clearly observed in the spectrum. These WGMs have different resonance Q-factors, extinction ratios (ERs), and free-spectral ranges (FSRs). The FSRs for modes A, B, and C are 17.59, 18.27 and 18.81 nm, respectively. As a higher-order WGM has its mode intensity distributed more towards the disk center, it has a larger FSR. Therefore, we could deduce that mode A is the lowest excited mode and mode C the highest. The Q-factor for mode A is ~6×10^4, higher than those of mode B (~3×10^4) and C (~8×10^3). From the resonance ER, we can see mode A is more approaching to critical coupling.

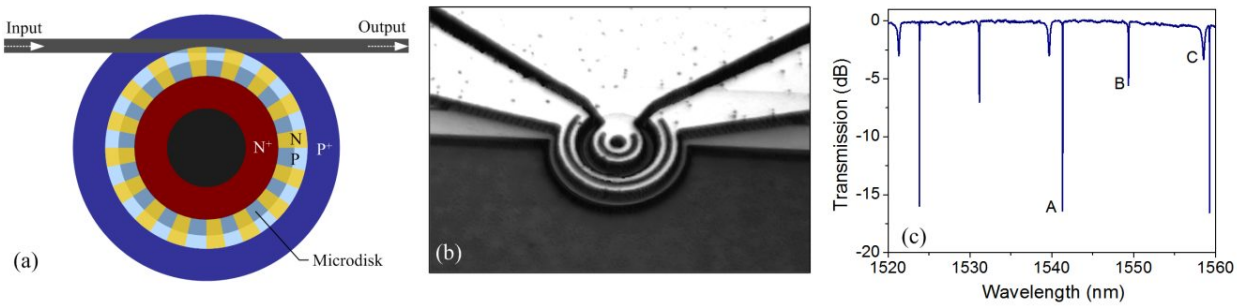

Figure 1. (a) Schematic of the tunable microdisk resonator. (b) Microscope image of the fabricated device. (c) Measured transmission spectrum. Three resonance modes A, B, and C are discerned.

Figure 2 shows the optical power and group delay spectra changing with both forward and reverse biases for the three WGMs. For a reverse bias, we apply a voltage onto the p-n junctions; for a forward bias, we inject a current instead and the voltage is in-situ monitored. The positive group delay of mode A at 0 V suggests it is over-coupled. With an increase of the negative voltage, the resonance A is red-shifted and the associated ER and group delay both reduce as seen from Figs. 2(a) and (b). The red-shift at -8V is 0.062 nm, more than one resonance width. Under a reverse bias, the depletion regions of the p-n junctions become wide, leading to an increase in mode effective index and reduction in loss. Therefore, it is more over-coupled with the increasing negative voltage, and hence the group delay reduces with an increased bandwidth. On the contrary, when a current flows through the p-n junctions, the resonance experiences a blue-shift instead. The blue-shift is more efficient than the red-shift. At 0.1 mA (0.894 V), resonance A is already blue-shifted by 0.19 nm. Since the refractive index change by free carrier injection is inevitably accompanied by absorption loss, the resonance ER and group delay incur a significant change. As seen from Fig. 2(b), the group delay is negative for forward biases, indicating the overall cavity loss exceeds the coupling and the microdisk works at the under-coupling regime. Mode B experiences a similar change trend with mode A as shown in Figs. 2(c) and (d). The critical coupling occurs between 0.1 and 0.2 mA current levels, since the group delay changes sign in between. At critical coupling, mode B has a lower Q-factor than mode A, which suggests mode B has stronger coupling with the access waveguide. For mode C, the scenario is quite different as illustrated in Figs. 2(e) and (f). The group delay is always negative no matter it is forward- or reverse-biased. Given its low Q-factor and under-coupling, we know it must have a high internal loss most probably due to its high overlap with the central N^+ doping.

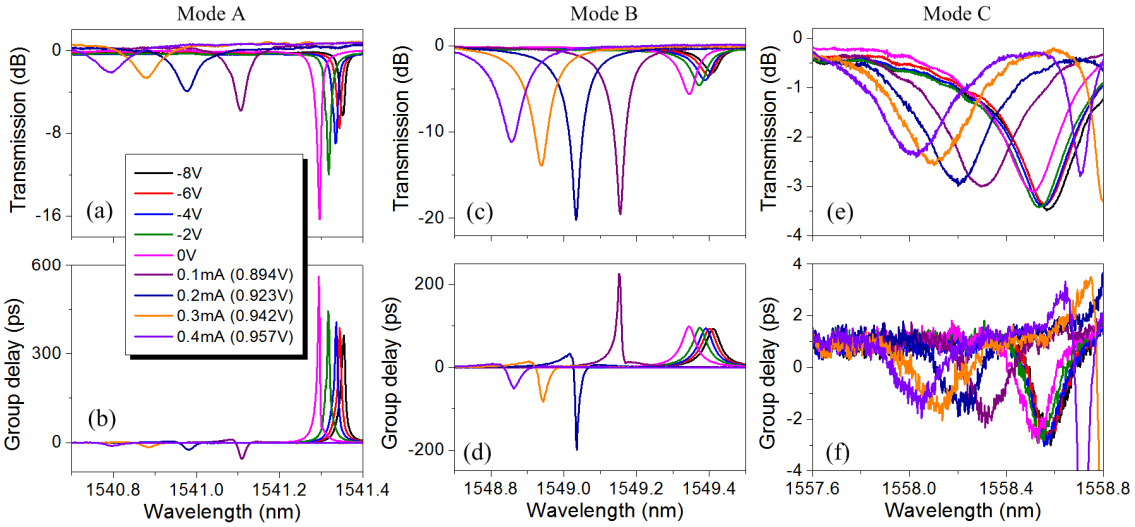

Figure 2. Change of transmission and group delay spectra with the reverse voltage and forward current for three WGMs. (a), (c), and (e) are the optical power transmission spectra. (b), (d), and (f) are the group delay spectra.

2.2 MZI-nested microring resonator

Besides tuning the resonator directly to get a desired resonance feature, coupling can also be utilized to control the resonance. To conveniently tune the coupling coefficient, we can use a tunable coupler to replace the static coupler [25]. Here we present a MZI-nested microring resonator with its resonance ER and group delay tunable.

Figure 3(a) shows the schematic graph of the device, consisting of a 2×2 MZI with its one output routed back to one input to form a ring resonator. The MZI is composed of a pair of 3-dB multimode interference (MMI) couplers. The MMI is 5-μm-wide and 31.5-μm-long. The waveguide width is 0.5 μm. If the two MZI arms have an equal length, then the coupling is 100%, which will not generate resonance. Therefore, we make the upper arm a little longer (close to π phase change at 1550 nm) so as to get weak coupling before tuning. 250 μm long lateral p-i-p junction based resistors are integrated in the MZI arms. The cross sectional schematic of the p-i-p resistor is shown in Fig. 3(b). The separation between the two P^+ regions is 1.7 μm. When current flows through the resistor, thermal heat will be generated therein, increasing the waveguide refractive index. This silicon based resistor is compatible with and does not add complexity to a typical p-n diode fabrication process. Figure 3(c) shows the optical microscope image of the fabricated device.

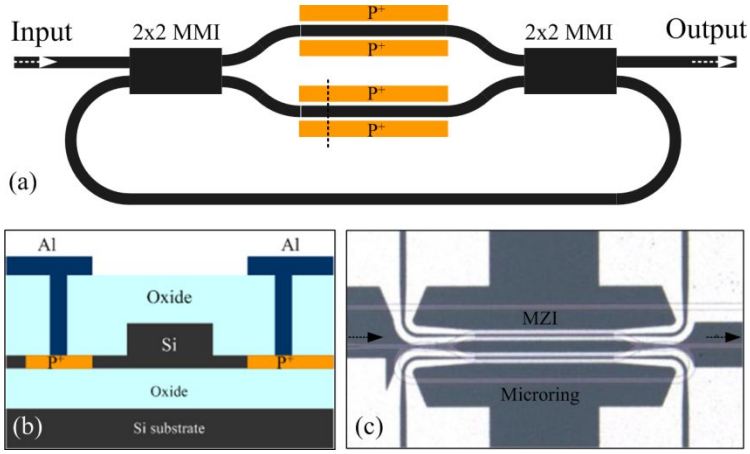

Figure 3. (a) Schematic of the MZI-nested microring resonator. (b) Cross-sectional schematic of the p-i-p resistor. (c) Optical microscope image of the fabricated device.

Figure 4(a) illustrates the measured transmission spectrum without tuning. Multiple resonance notches with a varying ER are observed. The ER is high near 1552 nm and gradually reduces towards both wavelength sides. The varying ER is resulted from the wavelength dependence of the MZI coupler. Figures 4(b) and (c) show the transmission power and group delay responses when the upper arm is tuned by a current source. Unlike a p-i-n diode where carrier concentration increases with current, the p-i-p resistor has a constant carrier level in the intrinsic region if the current is not too high. Therefore, the MZI does not suffer extra loss during thermal tuning. It can be seen that the ER and group delay vary with the current and the resonance is slightly red-shifted during the tuning. The maximum group delay is ~100 ps, achieved round 1555.5 nm at 0.4 mA current. Since both arms can be tuned simultaneously, the MZI coupler can work at push-pull mode, and then the group delay can be tuned whiling keeping the resonance wavelength fixed. This feature is useful in practical delay application, because the group delay dispersion is always zero at the fixed resonance wavelength.

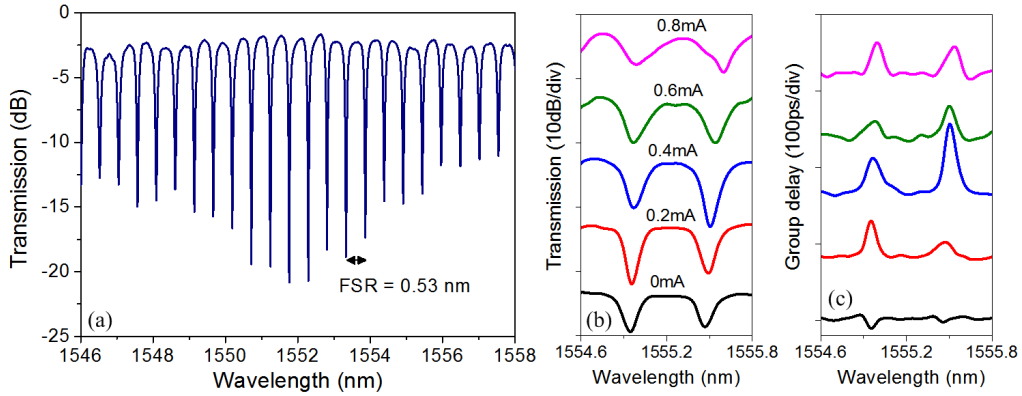

Figure. 4 (a) Measured transmission spectrum of the MZI-nested microring resonator without tuning. (b) Transmission power and (c) group delay spectra at various currents.

2.3 Cascaded SCOW resonators

In our previous work, we proposed and demonstrated novel SCOW resonators [26-29]. The SCOW resonators are distinct from conventional microring resonators in that clockwise (CW) and counter-clockwise (CCW) resonance modes are co-excited and energy transfer is unidirectional from one mode to the other. This unique characteristic results in many interesting features. For example, a single SCOW resonator can exhibit single-channel, dual-channel, or broad-stopband filtering features depending on the coupling coefficients [27]. As for cascaded SCOW resonators, the optical responses are more complicated, as Fabry-Perot resonances are also generated between two adjacent SCOW resonators due to resonant feedback [28]. As a result, electromagnetically-induced transparency (EIT)-like resonances appear in the transmission spectrum. The number of EIT peaks and their peak value are determined by the reflectivity of each

individual SCOW resonators as well as the phase of the connection waveguide. In this part, we present our recent experimental results on two-stage cascaded SCOW resonators.

Figure 5(a) shows the schematic structure of the cascaded SCOW resonators. The two individual SCOW resonators are symmetric and connected by a phase shifter in between. The waveguide width is 0.45 μm. The coupling lengths are L_{c1} = 8 μm and L_{c2} = 10 μm, and the coupling gap is 0.2 μm. The round-trip length of the SCOW resonators is 114.5 μm. The phase shifter length is 59 μm. The coupling coefficients of the two couplers determine the reflectivity of the SCOW resonator, and the phase shifter controls the frequency detuning between the SCOW and FP resonances. The phase shifter is based on a lateral p-i-p junction, the same as in the MZI-nested microring resonator (see subsection 2.2). Figure 5(b) is the optical microscope image of the fabricated device.

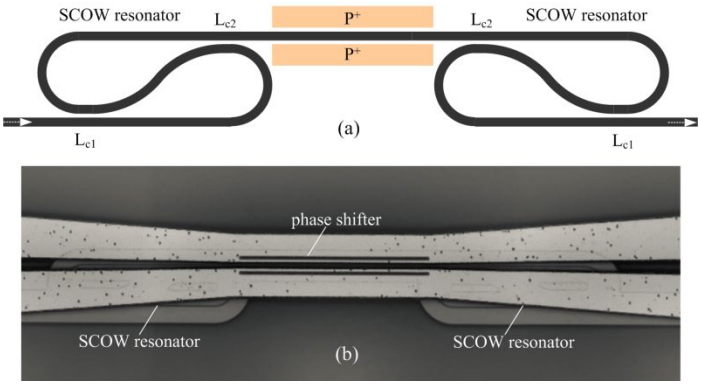

Figure 5. (a) Schematic of the cascaded SCOW resonators. (b) Optical microscope image of the fabricated device.

Figure 6(a) depicts the measured transmission and reflection spectra. The resonance FSR is 5.1 nm. EIT-like resonance features can be discerned from the spectra. The zoom-in spectra around 1538 nm are shown in Fig. 6(b). Two pronounced sharp EIT peaks reside in a broad reflection band with Q-factors of 4.5×10^4 and 6.3×10^4. They are separated by 0.23 nm. The right EIT peak is closer to the SCOW resonance wavelength, and hence the SCOW reflection could be higher, leading to a higher Q-factor. It should be noted that there is a third EIT-like resonance around 1538.5 nm and somehow it becomes a dip in the transmission. This is probably due to the interference with background signals. We also measured the group delay responses at the transmission and reflection ends as shown in Fig. 6(c). Three group delay peaks exist in one FSR corresponding to the three EIT resonances. The left EIT resonance from the reflection end has the highest group delay. The inset in Fig. 6(c) shows the tuning of the group delay peak at 1538 nm. At 8 mA current, the peak red-shifts by 7 pm, inducing a 300 ps delay reduction at the initial resonance wavelength.

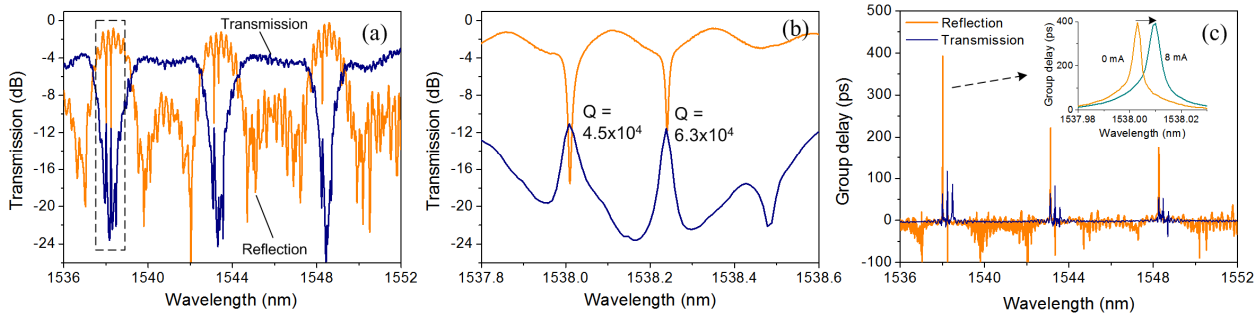

Figure. 6 (a) Measured transmission and reflection spectra of the cascaded SCOW resonators without tuning. (b) Zoom-in of the EIT-like resonance spectra. (c) Group delay responses at the transmission and reflection ends. Inset shows the group delay tuning with current.

2.4 Athermal MZI lattice filter

Integrated photonic devices based on silicon waveguides always suffer a temperature sensitivity issue. Silicon has a large thermo-optic (TO) coefficient of ~1.86×10^{-4} K^{-1} around 1.55 μm, resulting in a considerable thermal drift for regular devices. For example, a typical silicon microring resonator has a temperature sensitivity of ~110 pm/K [30]. The temperature dependence of silicon photonic devices makes them unsuitable for many practical applications. To alleviate

such a thermal sensitivity problem, hybrid waveguide systems like polymer-clad silicon slot waveguides can be employed [31]. However, the introduction of exotic materials makes the fabrication complicated and CMOS-incompatible. A more attractive way to make thermally-stable devices is to play tricks on the design level. By making use of the difference in their effective TO coefficients of silicon waveguides with different widths, MZIs and MZI-coupled microring resonators were demonstrated to have a low thermal sensitivity [30, 32]. Along this line, we designed a tunable lattice filter composed of 10 athermal MZIs. Compared with a single MZI filter, the lattice filter has the advantages of narrower passband and higher extinction ratio.

Figure 7(a) shows the schematic structure of our tunable lattice filter. The 10 MZI units are identical and designed to have an athermal response near 1550 nm. The up arm of the MZI is formed by a thin waveguide of 350 nm wide with an effective length of L_1 and the bottom arm is a regular waveguide of 500 nm wide with an effective length of L_2. Phase shifters based on lateral p-i-p resistors are integrated in both arms. Figure 7(b) shows the optical micrograph of the fabricated device. The up and bottom arms of the 10 MZI units are connected by two separate metal lines.

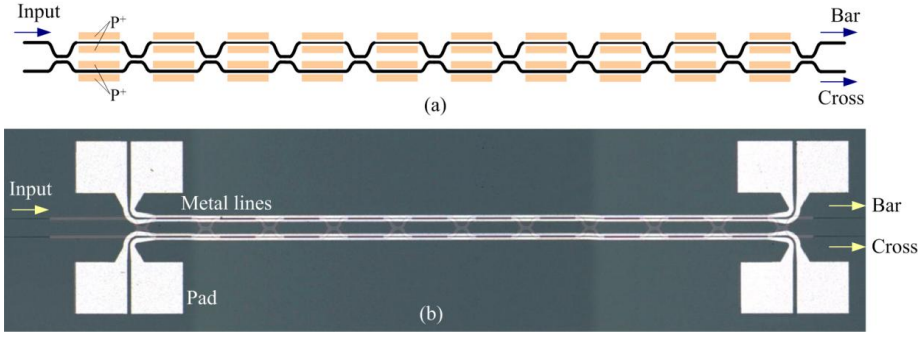

Figure 7. (a) Schematic of the athermal lattice filter. (b) Optical microscope image of the fabricated device.

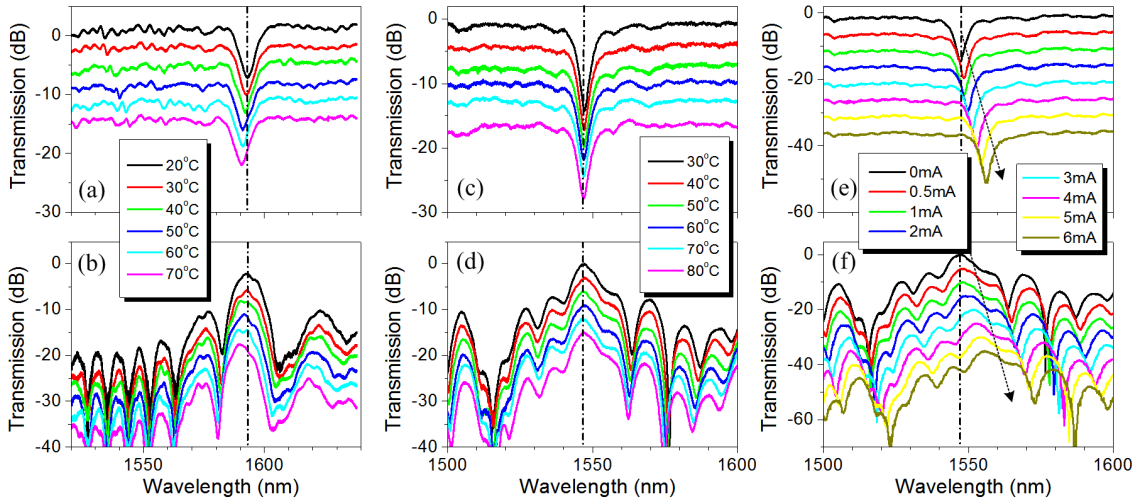

Figure 8. (a) and (b) Thermal shift of transmission spectra for a lattice filter with L_1 = 106.4 μm, L_2 = 100 μm, and g = 300 nm. (c) and (d) Thermal shift of transmission spectra for another lattice filter with L_1 = 107.4 μm, L_2 = 100 μm, and g = 250 nm. (e) and (f) Tuning of transmission spectra with various currents applied to the upper arms. The upper plots are for the bar-port and bottom ones for the cross-port.

In our measurement, light was input from the left upper port and the two right ports (denoted as bar- and cross-ports) were measured. A thermoelectric cooler (TEC) was put under the device to control its temperature. We first characterized a device with L_1 = 106.4 μm and L_2 = 100 μm. The coupling gap is g = 300 nm, corresponding to a power coupling coefficient of 0.015. Figures 8(a) and (b) show the measured transmission spectra under various temperatures for the bar- and cross-ports, respectively. The passband central wavelength is around 1590 nm. The passband slightly shifts to the short wavelength side with the increase of temperature. The temperature sensitivity is -51 pm/K. It is expected since the athermal operation point is designed to be around 1550 nm. Figures 8(c) and (d) show the

transmission spectra for another device. The arm lengths are L_1 = 107.4 μm and L_2 = 100 μm. The coupling gap is g = 250 nm, corresponding to an increased power coupling coefficient of 0.028. For this device, the passband is around 1550 nm and it is almost fixed with its temperature sensitivity lowered to 6 pm/K. It is interesting to note that the sidelobes beside the passband moves toward the central wavelength with the increasing temperature. We applied a current to the upper arms to tune the passband as shown in Figs. 8(e) and (f). The passband shifts to the longer wavelength side with the increasing current. The average tuning efficiency is 1.5 nm/mA. In our current design, the MZI units are all set identical, which is not an optimal design. In fact, a lattice filter with a flat-top passband and a high rejection ratio could be obtained if we optimize the coupling coefficients using a filter synthesis algorism [33].

3. CONCLUSIONS

In summary, we presented our recent progress on tunable silicon photonic devices. Four devices were discussed including the tunable microdisk resonator, the MZI-nested microring resonator, the cascaded SCOW resonators, and the athermal MZI lattice filter. In the tunable microdisk resonator, interleaved p-n junctions are used facilitating convenient resonance tuning. The resonance is red-shifted by 0.062 nm at a reverse voltage of -8 V, and blue-shifted by 0.19 nm at a forward current of 0.1 mA. The mode dependence of the resonance spectrum and group delay was also discussed. In the MZI-nested microring resonator, we demonstrated another resonance tuning approach that is by controlling its coupling with the access waveguide. In this way, the filter notch depth and group delay can be varied with the central wavelength almost fixed. A p-i-p junction based integrated resistor is used to thermally tune the coupling. We also presented novel cascaded SCOW resonators. EIT-like resonances are generated featuring a high Q-factor of 6×10^4 comparable to the microdisk resonator. Group delay response and its tuning were also characterized. To address the temperature sensitivity issue in silicon optical filters, we designed an athermal lattice filter by manipulating the MZI arm waveguide width. Experimental results show that the temperature sensitivity can be suppressed to 6 pm/K, and meanwhile, the passband can still be tuned by an integrated local thermal heater. The devices presented in this paper were all fabricated in a CMOS foundry with the same process. In our next step, we would like to integrate the discrete components to make functional photonic circuits for on-chip optical information processing.

4. ACKNOWLEDGEMENTS

This work was supported in part by 973 program (ID2011CB301700), the National Natural Science Foundation of China (NSFC) (61007039, 61001074), the Science and Technology Commission of Shanghai Municipality (STCSM) Project (10DJ1400402, 12XD1406400). We also acknowledge IME Singapore for device fabrication.

REFERENCES

[1] C. Batten, A. Joshi, J. Orcutt, A. Khilo, B. Moss, C. W. Holzwarth, M. A. Popovic, H. Li, H. I. Smith, and J. L. Hoyt, "Building many-core processor-to-DRAM networks with monolithic CMOS silicon photonics," IEEE Micro **29**, 8-21 (2009).

[2] M. Asghari and A. V. Krishnamoorthy, "Silicon photonics: Energy-efficient communication," Nat. Photonics **5**, 268-270 (2011).

[3] Y. A. Vlasov, "Silicon CMOS-integrated nano-photonics for computer and data communications beyond 100G," IEEE Comm. Mag. **50**, s67-s72 (2012).

[4] P. Dumon, W. Bogaerts, R. Baets, J. M. Fedeli, and L. Fulbert, "Towards foundry approach for silicon photonics: silicon photonics platform ePIXfab," Electron. Lett. **45**, 581-582 (2009).

[5] L. Tsybeskov, D. J. Lockwood, and M. Ichikawa, "Silicon Photonics: CMOS Going Optical," Proc. IEEE **97**, 1161-1165 (2009).

[6] S. S. Djordjevic, L. W. Luo, S. Ibrahim, N. K. Fontaine, C. Poitras, B. Guan, L. Zhou, K. Okamoto, Z. Ding, and M. Lipson, "Fully reconfigurable silicon photonic lattice filters with four cascaded unit cells," IEEE Photon. Technol. Lett. **23**, 42-44 (2011).

[7] L. Zhou and A. W. Poon, "Electrically reconfigurable silicon microring resonator-based filter with waveguide-coupled feedback," Opt. Express **15**, 9194-9204 (2007).

[8] M. Yang, W. M. J. Green, S. Assefa, J. Van Campenhout, B. G. Lee, C. V. Jahnes, F. E. Doany, C. L. Schow, J. A. Kash, and Y. A. Vlasov, "Non-blocking 4x4 electro-optic silicon switch for on-chip photonic networks," Opt. Express **19**, 47-54 (2011).
[9] P. Cheben, J. Schmid, A. DelÔge, A. Densmore, S. Janz, B. Lamontagne, J. Lapointe, E. Post, P. Waldron, and D. X. Xu, "A high-resolution silicon-on-insulator arrayed waveguide grating microspectrometer with sub-micrometer aperture waveguides," Opt. Express **15**, 2299-2306 (2007).
[10] F. Gardes, D. Thomson, N. Emerson, and G. Reed, "40 Gb/s silicon photonics modulator for TE and TM polarisations," Opt. Express **19**, 11804-11814 (2011).
[11] D. J. Thomson, F. Y. Gardes, J. M. Fedeli, S. Zlatanovic, Y. Hu, B. P. P. Kuo, E. Myslivets, N. Alic, S. Radic, and G. Z. Mashanovich, "50-Gb/s silicon optical modulator," IEEE Photon. Technol. Lett. **24**, 234-236 (2012).
[12] X. Xiao, H. Xu, X. Li, Y. Hu, K. Xiong, Z. Li, T. Chu, Y. Yu, and J. Yu, "25 Gbit/s silicon microring modulator based on misalignment-tolerant interleaved PN junctions," Opt. Express **20**, 2507-2515 (2012).
[13] L. Zhou and A. W. Poon, "Silicon electro-optic modulators using pin diodes embedded 10-micron-diameter microdisk resonators," Opt. Express **14**, 6851-6857 (2006).
[14] P. De Dobbelaere, S. Abdalla, S. Gloeckner, M. Mack, G. Masini, A. Mekis, T. Pinguet, S. Sahni, A. Narasimha, and D. Guckenberger, "Si Photonics Based High-Speed Optical Transceivers," in *European Conference and Exhibition on Optical Communication (ECOC)*, (Optical Society of America, 2012),
[15] A. Narasimha, B. Analui, Y. Liang, T. J. Sleboda, S. Abdalla, E. Balmater, S. Gloeckner, D. Guckenberger, M. Harrison, and R. G. M. P. Koumans, "A fully integrated 4×10-Gb/s DWDM optoelectronic transceiver implemented in a standard 0.13 μm CMOS SOI technology," IEEE J. Solid-State Circuits **42**, 2736-2744 (2007).
[16] C. T. DeRose, D. C. Trotter, W. A. Zortman, A. L. Starbuck, M. Fisher, M. R. Watts, and P. S. Davids, "Ultra compact 45 GHz CMOS compatible Germanium waveguide photodiode with low dark current," Opt. Express **19**, 24897-24904 (2011).
[17] R. E. Camacho-Aguilera, Y. Cai, N. Patel, J. T. Bessette, M. Romagnoli, L. C. Kimerling, and J. Michel, "An electrically pumped germanium laser," Opt. Express **20**, 11316-11320 (2012).
[18] G. Roelkens, L. Liu, D. Liang, R. Jones, A. Fang, B. Koch, and J. Bowers, "III‐V/silicon photonics for on‐chip and intra‐chip optical interconnects," Laser Photon. Rev. **4**, 751-779 (2010).
[19] W. Bogaerts, P. De Heyn, T. Van Vaerenbergh, K. De Vos, S. Kumar Selvaraja, T. Claes, P. Dumon, P. Bienstman, D. Van Thourhout, and R. Baets, "Silicon microring resonators," Laser Photon. Rev. **6**, 47-73 (2011).
[20] M. Soltani, S. Yegnanarayanan, and A. Adibi, "Ultra-high Q planar silicon microdisk resonators for chip-scale silicon photonics," Opt. Express **15**, 4694-4704 (2007).
[21] I. Giuntoni, D. Stolarek, D. I. Kroushkov, J. Bruns, L. Zimmermann, B. Tillack, and K. Petermann, "Continuously tunable delay line based on SOI tapered Bragg gratings," Opt. Express **20**, 11241-11246 (2012).
[22] T. Baba, "Slow light in photonic crystals," Nat. Photonics **2**, 465-473 (2008).
[23] P. Dong, W. Qian, H. Liang, R. Shafiiha, N. N. Feng, D. Feng, X. Zheng, A. V. Krishnamoorthy, and M. Asghari, "Low power and compact reconfigurable multiplexing devices based on silicon microring resonators," Opt. Express **18**, 9852-9858 (2010).
[24] R. Soref and B. Bennett, "Electrooptical effects in silicon," IEEE J. Quantum Electron. **23**, 123-129 (1987).
[25] A. Yariv, "Critical coupling and its control in optical waveguide-ring resonator systems," IEEE Photon. Technol. Lett. **14**, 483-485 (2002).
[26] L. Zhou, T. Ye, and J. Chen, "Coherenet interference induced transparency in self-coupled optical waveguide-based resonators," Opt. Lett. **36**, 13-15 (2011).
[27] X. Sun, L. Zhou, X. Li, Z. Hong, J. Xie, H. Zhu, Z. Zou, L. Lu, and J. Chen, "Experimental demonstration of self-coupled optical waveguide (SCOW)-based resonators," in *17th OptoElectronics and Communications Conference (OECC),* (Busan, Korea, 2012).
[28] L. Zhou, J. Chen, X. Sun, J. Xie, and H. Zhu, "Optical signal processing using silicon resonance and slow-light structures," in *SPIE Photonics West (Silicon Photonics VII)*, (SPIE, 2012), 82660N.
[29] L. Zhou, J. Xie, L. Lu, Z. Zou, X. Sun, and J. Chen, "Coupled-resonator-induced-transparency in cascaded self-coupled optical waveguide (SCOW) resonators," in *the Asia Communications and Photonics Conference (ACP)* 2012.
[30] B. Guha, B. B. C. Kyotoku, and M. Lipson, "CMOS-compatible athermal silicon microring resonators," Opt. Express **18**, 3487-3493 (2010).
[31] L. Zhou, K. Okamoto, and S. J. B. Yoo, "Athermalizing and trimming of slotted silicon microring resonators with UV-sensitive PMMA upper-cladding," IEEE Photon.Technol. Lett. **21**, 1175-1177 (2009).

[32] B. Guha, A. Gondarenko, and M. Lipson, "Minimizing temperature sensitivity of silicon Mach-Zehnder interferometers," Opt. Express **18**, 1879-1887 (2010).
[33] C. K. Madsen and J. H. Zhao, *Optical filter design and analysis: a signal processing approach* (John Wiley & Sons, Inc., 1999).